Noise-optimized virtual monoenergetic dual-energy computed tomography: optimization of kiloelectron volt settings in patients with gastrointestinal stromal tumors

Simon S. Martin,[1] Sophia Pfeifer,[1] Julian L. Wichmann,[1] Moritz H. Albrecht,[1,2]
Doris Leithner,[1] Lukas Lenga,[1] Jan-Erik Scholtz,[1,3] Thomas J. Vogl,[1] Boris Bodelle[1]

[1]Department of Diagnostic and Interventional Radiology, University Hospital Frankfurt, Theodor-Stern-Kai 7, 60590 Frankfurt, Germany
[2]Department of Radiology and Radiological Science, Medical University of South Carolina, Charleston, SC, USA
[3]Cardiac MR PET CT Program, Harvard Medical School, Massachusetts General Hospital, Boston, MA, USA

Abstract

Purpose: The aim of this study was to evaluate the impact of a noise-optimized virtual monoenergetic imaging (VMI+) reconstruction technique on quantitative and qualitative image analysis in patients with gastrointestinal stromal tumors (GISTs) at dual-energy computed tomography (DECT) of the abdomen.
Methods: Forty-five DECT datasets of 21 patients (14 men; 63.7 ± 9.2 years) with GISTs were reconstructed with the standard linearly blended (M_0.6) and VMI+ and traditional virtual monoenergetic (VMI) algorithm in 10-keV increments from 40 to 100 keV. Attenuation measurements were performed in GIST lesions and abdominal metastases to calculate objective signal-to-noise (SNR) and contrast-to-noise ratios (CNR). Five-point scales were used to evaluate overall image quality, lesion delineation, image sharpness, and image noise.
Results: Quantitative image parameters peaked at 40-keV VMI+ series (SNR 27.8 ± 13.0; CNR 26.3 ± 12.7), significantly superior to linearly blended (SNR 16.8 ± 7.3; CNR 13.6 ± 6.9) and all VMI series (all $P < 0.001$). Qualitative image parameters were highest for 60-keV VMI+ reconstructions regarding overall image quality and image sharpness (median 5, respectively; $P \leq 0.023$). Qualitative assessment of lesion delineation peaked in 40 and 50-keV VMI+ series (median 5, respectively). Image noise was superior in 90 and 100-keV VMI and VMI+ reconstructions (all medians 5).

Conclusions: Low-keV VMI+ reconstructions significantly increase SNR and CNR of GISTs and improve quantitative and qualitative image quality of abdominal DECT datasets compared to traditional VMI and standard linearly blended image series.

Key words: Dual-energy CT—Virtual monoenergetic imaging—Gastrointestinal stromal tumor—Image quality—Oncology

Correspondence to: Julian L. Wichmann; *email:* docwichmann@gmail.com

Gastrointestinal stromal tumors (GISTs) constitute the most common mesenchymal tumors that typically arise from the wall of the gastrointestinal (GI) tract. Most GISTs (70–80%) are benign; however, there is a continuum of variable malignant potential, ranging from small lesions with benign characteristics to malignant sarcomas [1, 2]. About 50% of the patients with malignant GISTs present with metastatic disease at the time of diagnosis [3]. The most frequent location of primary GISTs is the stomach, followed by the small intestine, colon, and rectum, whereas the liver constitutes the predominant location of GIST metastases, followed by the peritoneum [3–5]. Contrast-enhanced CT of the abdomen and pelvis remains the standard imaging method for staging and follow-up of patients with GISTs. During treatment, GIST lesions and metastases may show a decreasing tumor density or hypovascularization in the case of therapeutic success [6]. Moreover, measuring the tumor size and density on contrast-enhanced CT in GIST patients provides a reproducible and precise method for

evaluating tumor response and has been adopted into clinical practice, in the form of the Choi criteria [7].

Dual-energy CT (DECT) offers several post-processing techniques facilitating an optimized evaluation of GIST patients, e.g., the calculation of virtually non-enhanced images used to reduce the radiation dose and the calculation of iodine maps as a visual support to identify enhancing lesions [8, 9]. Moreover, reconstruction of virtual monoenergetic images (VMI) is a promising technique that enables an improved iodine signal at low-keV levels which may improve lesion delineation due to increased contrast [10, 11]. In the recent past, a noise-optimized virtual monoenergetic reconstruction algorithm (VMI +) has been developed to reduce image noise at low-keV levels while maintaining an increased contrast enhancement similar to its predecessor. The VMI + algorithm performs a regional spatial frequency-based recombination of high attenuation at lower energy levels and reduced image noise at higher energies to obtain the best possible image contrast [12]. This reconstruction technique has shown favorable results in prior studies evaluating vascular and oncologic imaging [12–17]. However, noise-optimized VMI + has not been applied to assess image quality in staging and follow-up of GISTs so far.

Materials and methods

Patient population

This retrospective study was approved by the ethics committee of our university hospital, and the requirement for written informed consent was waived. The study group consisted of 21 patients treated for histologically proven GIST. All patients had undergone clinically indicated staging or follow-up DECT examinations between August 2014 and June 2016.

General exclusion criteria for DECT imaging were known allergies to iodinated contrast material, pregnancy, age younger than 18 years, and impaired renal function (glomerular filtration rate < 45 ml/min). Moreover, DECT examinations with severe motion artifacts, contrast material extravasation, and examinations with deviations from the standard contrast media injection protocol were excluded.

DECT image acquisition

All CT examinations of the abdomen were performed on a third-generation dual-source DECT scanner (SOMATOM Force, Siemens Healthcare, Erlangen, Germany). Image acquisition during the portal-venous phase started automatically 60 s after contrast material injection in craniocaudal direction and inspiratory breathhold. A non-ionic contrast agent (Imeron 400, Bracco, Milan, Italy) at a dose of 1.2 ml per kilogram body weight was injected at a flow rate of 3 ml/s through a peripheral vein of the forearm. Settings for the DECT mode were as follows: tube A 90 kV, reference current–time product of 95 mAs per rotation; tube B Sn150 kV with tin filter, 59 mAs per rotation. Rotation time was 0.25 s, pitch was set to 0.7 and collimation to $2 \times 192 \times 0.6$ mm. Scans were acquired using attenuation-based tube current modulation (CARE Dose 4D, Siemens). The volume CT dose index (CTDI$_{vol}$) and the dose length product (DLP) of each patient were recorded for an estimation of the DECT radiation dose.

DECT image reconstruction

DECT raw data were post-processed on a 3D multimodality workstation (syngo.via, version VA30A, Siemens) using a soft tissue convolution kernel (Qr40, Siemens) and iterative reconstruction technique (ADMIRE, Siemens; strength level, 3). Standard image series with linear blending technique (M_0.6) were automated and reconstructed by merging 60% of the low with 40% of the high-kV data to emulate routine single-energy 120-kV acquisition [13, 15, 18]. The traditional VMI and noise-optimized VMI + series were reconstructed at 40–100 keV levels in 10-keV intervals. Calculation of each monoenergetic image series at a specific energy level requires approximately 1 min of manual input to reconstruct and transfer images to the picture archiving and communication system. In accordance with prior studies, images at higher energy levels beyond 100 keV were not calculated, as the iodine attenuation can be expected to be too low [19]. All series were reconstructed as axial and coronal slices, with a thickness and increment of 1.5 mm, respectively.

Quantitative image analysis

For the evaluation of quantitative image quality, image series were reviewed by a radiologist with 3 years of experience in CT, who did not take part in the subsequent image interpretation. Signal attenuation in mean HU and image noise, defined as the standard deviation (SD) of fat, were measured in GIST lesions and metastases as well as in the tumor feeding artery to evaluate tumor vascularization. The corresponding tumor feeding arteries were as follows: the celiac artery, the superior mesenteric artery, the gastric arteries, the inferior mesenteric artery, and the internal iliac arteries. In case of liver or peritoneal metastases, measurements were implemented in the hepatic artery and superior mesenteric artery, respectively. Measurements were performed by placing a circular region-of-interest centrally in the tumor lesion (100 mm^2). Focal areas of tumor necrosis were avoided. Additional measurements were performed within the psoas muscle (250 mm^2) and subcutaneous fat at the lower back (250 mm^2) to assess image contrast and background noise. Measurements were performed three

times and averaged to ensure data consistency and keep measuring inaccuracies as low as possible.

For calculating signal-to-noise ratio (SNR) and contrast-to-noise ratio (CNR) values, the following formulas were used according to previous studies [15, 20, 21]:

$$SNR = \frac{HU\ (lesion)}{SD\ (fat)}$$

$$CNR = \frac{HU\ (lesion) - HU\ (muscle)}{SD\ (fat)}.$$

Qualitative image analysis

Three radiologists with 3–6 years of experience independently assessed all DECT images and were blinded to the DECT image reconstruction technique. Furthermore, readers were allowed to freely modify the preset window settings (width, 400 HU; level, 100 HU) as low-keV VMI + reconstructions may require different width and level settings to improve the visualization and contrast conditions in abdominal DECT [22]. The order of the different image series was randomized and only a single image series of each patient was evaluated at each reading session. In addition, a time interval of two weeks was kept between each read-out to prevent potential recall bias. Observers were aware that all patients received treatment for biopsy-proven GIST. Image series were rated using 5-point Likert scales under the following aspects [14]: Overall image quality (ranging from 1 = poor image quality with substantial image noise to 5 = excellent image quality with no perceivable noise), lesion delineation (ranging from 1 = no visual delineation to 5 = perfect delineation of contours), image sharpness (ranging from 1 = distinct blurring to 5 = no apparent blurring), and image noise (ranging from 1 = extensive image noise to 5 = absence of noise).

Statistical evaluation

Analyses were performed using dedicated statistical software (MedCalc Statistical Software Version 16.8, MedCalc Software bvba, Ostend, Belgium). Continuous variables were expressed as mean ± SD. Ordinal variables were reported as median with ranges. A P value < 0.05 was considered to indicate a statistically significant difference. The Kolmogorov–Smirnov test was applied to test for normality of data distribution. Data showing a continuous normal distribution were analyzed using the analysis of variance test. Multiple comparisons were accounted by Bonferroni correction. In the case of non-normal distribution, comparisons were performed using the Wilcoxon matched pairs test.

Interobserver agreement among reviewers was evaluated using intraclass correlation coefficient (ICC) statistics and interpreted in the following way: ICC < 0.20 = slight agreement, ICC 0.21–0.40 = fair

agreement, ICC 0.41–0.60 = moderate agreement, ICC 0.61–0.80 = substantial agreement, ICC 0.81–1.0 = almost perfect agreement [23].

Results

Study population

In this study, 45 consecutive DECT examinations (13 initial staging examinations and 32 follow-up examinations) of 21 patients with GISTs (mean age 63.4 ± 9.2 years; range 35–81 years) were analyzed, including 12 men (65.2 ± 7.9 years; range 41–81 years) and 9 women (61.0 ± 10.2 years; range 35–77 years). The patients' mean body mass index was 26.0 ± 3.3 kg/m^2, ranging from 20.7 to 35.9 kg/m^2. Mean cumulative CT dose index (CTDI$_{vol}$) of all examinations was 9.3 ± 4.4 mGy. Average cumulative DLP was 341.3 ± 249.5 mGy cm.

In 45 DECT examinations, a total of 76 GIST lesions and metastases were found (mean number of lesions per patient, 1.7; range 1–5). The primary tumor locations were the small bowel ($n = 24$), stomach ($n = 15$), rectum ($n = 3$), and the colon ($n = 3$). Metastases were seen in 27 examinations. The liver was involved in isolation in 18 examinations, while peritoneal metastases were present in 7. In 2 examinations, disease at both sites was observed. One patient showed multiple liver and peritoneal lesions with a total number of 4 metastases.

Quantitative image analysis

For quantitative image analysis, all 76 visible GIST lesions and metastases were evaluated. The 40-keV VMI and VMI + image series showed the highest mean attenuation in GIST lesions and metastases (371.8 ± 162.6 HU and 384.4.4 ± 153.4 HU, respectively; $P = 0.140$), whereas corresponding image noise at 40-keV VMI + (88.1 ± 58.4 HU) was significantly lower compared to the 40-keV VMI datasets (181.6 ± 13.3 HU; $P < 0.001$). Mean attenuation and image noise for the standard M_0.6 image series was 238.9 ± 87.5 and 58.6 ± 33.4 HU, respectively. The lowest noise was found for VMI and VMI + reconstructions at 100 keV (28.9 ± 11.8 and 18.5 ± 11.2 HU, respectively).
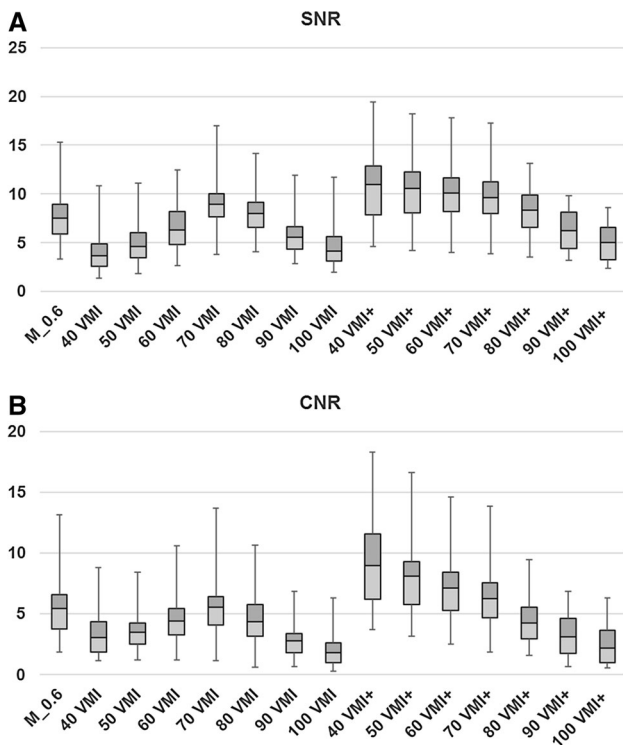
The calculated SNR and CNR in GIST lesions and metastases values were superior in the 40-keV VMI + series (SNR 11.0 ± 4.7; CNR 9.0 ± 4.1) and were significantly higher compared to standard linearly blended M_0.6 series (SNR 7.5 ± 2.8; CNR 5.5 ± 2.7) and all other monoenergetic image reconstructions ($P < 0.001$). In the traditional VMI series, highest SNR and CNR values were found at 70-keV (SNR 8.9 ± 3.0; CNR 5.5 ± 2.8) with no significant differences in comparison with M_0.6 image series ($P \geq 0.092$) but significantly lower than VMI + reconstructions at 40–70 keV ($P \leq 0.004$). Results of quantitative image quality assessment are summarized in Table 1 and Fig. 1.

Table 1. Comparison of quantitative image parameters

	M_0.6	40 VMI	50 VMI	60 VMI	70 VMI	80 VMI	90 VMI	100 VMI
Attenuation								
Artery (HU)	541.7 ± 72.8	926.8* ± 189.2	615.9* ± 106.9	426.8* ± 58.5	310.2* ± 32.9	235.2* ± 25.3	185.3* ± 27.8	150.8* ± 32.7
GIST (HU)	238.9 ± 58.6	371.8* ± 181.6	258.9 ± 103.7	190.3* ± 57.6	148.0* ± 32.8	120.9* ± 24.0	102.6* ± 24.9	90.1* ± 28.9
SNR								
Average SNR	12.1 ± 3.4	6.5* ± 3.8	7.8* ± 3.5	10.3* ± 3.6	13.9* ± 4.1	11.8 ± 2.9	7.7* ± 2.3	5.5* ± 2.2
Artery SNR	16.6 ± 3.9	9.4* ± 5.3	11.0* ± 4.7	14.3* ± 4.6	18.8* ± 5.2	15.6 ± 3.4	9.9* ± 2.6	6.8* ± 2.4
GIST SNR	7.5 ± 2.8	3.7* ± 2.2	4.6* ± 2.3	6.3* ± 2.5	8.9* ± 3.0	8.0 ± 2.4	5.5* ± 2.1	4.2* ± 2.1
CNR								
Average CNR	10.1 ± 3.2	5.9* ± 3.5	6.7* ± 3.2	8.3* ± 3.3	10.5 ± 3.8	8.1* ± 2.8	4.9* ± 1.9	4.1* ± 1.6
Artery CNR	14.8 ± 3.7	8.7* ± 5.0	9.9* ± 4.4	12.3* ± 4.3	15.4* ± 4.9	11.9* ± 3.3	7.0* ± 2.2	6.4* ± 1.8
GIST CNR	5.5 ± 2.7	3.0* ± 2.0	3.5* ± 2.0	4.4* ± 2.3	5.5 ± 2.8	4.3* ± 2.3	2.8* ± 1.6	1.8* ± 1.4

	40 VMI+	50 VMI+	60 VMI+	70 VMI+	80 VMI+	90 VMI+	100 VMI+
Attenuation							
Artery (HU)	930.2* ± 109.9	622.2* ± 73.4	435.5* ± 51.3	320.4* ± 37.7	246.0* ± 29.0	192.7* ± 24.2	157.1* ± 21.8
GIST (HU)	384.4* ± 88.1	269.4* ± 59.8	199.4 ± 42.7	156.3* ± 32.2	128.2* ± 25.3	108.8* ± 20.8	95.3* ± 18.5
SNR							
Average SNR	18.8* ± 5.7	17.5* ± 7.8	16.1* ± 4.1	14.7* ± 3.5	13.0 ± 2.8	8.7* ± 2.3	6.7* ± 2.1
Artery SNR	26.6* ± 6.7	24.5* ± 11.4	22.1* ± 4.8	19.8* ± 4.0	17.6 ± 3.3	11.1* ± 2.5	8.5* ± 2.0
GIST SNR	11.0* ± 4.7	10.6* ± 4.2	10.1* ± 3.5	9.6* ± 3.1	8.3* ± 2.4	6.2* ± 2.1	5.0* ± 2.1
CNR							
Average CNR	16.9* ± 5.3	15.1* ± 4.6	13.2* ± 3.8	11.3 ± 3.3	9.0 ± 2.5	5.6* ± 2.2	4.7* ± 1.8
Artery CNR	24.8* ± 6.5	22.1* ± 5.5	19.2* ± 4.5	16.4* ± 3.7	13.7 ± 3.1	8.1* ± 2.5	7.2* ± 1.9
GIST CNR	9.0* ± 4.1	8.1* ± 3.6	7.1* ± 3.2	6.2 ± 2.9	4.2 ± 2.0	3.1* ± 1.9	2.2* ± 1.7

Mean attenuation, signal-to-noise ratio (SNR), and contrast-to-noise ratio (CNR) of GISTs and the afferent artery were compared between standard linearly blended dual-energy CT (DECT) series (M_0.6), traditional virtual monoenergetic images (VMI), and noise-optimized VMI+ reconstructions at different keV levels
* Significant difference compared to M_0.6 images. Attenuation values are given in HU

Fig. 1. Box-and-whisker plots show average signal-to-noise (SNR; **A**) and contrast-to-noise ratios (CNR; **B**) in GIST lesions and metastases compared between standard linearly blended, traditional VMI, and the noise-optimized VMI+ reconstructions at various keV levels. *Boxes* represent the interquartile range Q1 to Q3, *horizontal lines* within mark the median values, and the whiskers represent minimal and maximal values. VMI values are given in keV. SNR and CNR were superior in the 40-keV VMI+ image series (SNR 11.0 ± 4.7; CNR 9.0 ± 4.1) and were significantly higher compared to all VMI and standard M_0.6 series ($P < 0.001$).

Qualitative image analysis

Ratings for overall subjective image quality were highest for 60-keV VMI+ reconstructions (median 5; $P ≤ 0.008$) with substantial interrater agreement [ICC 0.70; 95% confidence intervals (CI) 0.49–0.86]. Images reconstructed with the traditional VMI algorithm revealed highest overall subjective image quality ratings at 70-keV with substantial interrater agreement (median 4; ICC 0.61; 95% CI 0.35–0.79). VMI+ images with energy levels ranging from 50 to 70-keV and VMI images at 70 keV received superior overall image quality ratings compared to linearly blended M_0.6 images (median 3; $P ≤ 0.015$).

Subjective evaluation of lesion delineation peaked at 40 and 50-keV VMI+ (both medians 4) with almost perfect interrater agreement in both series (ICC 0.82; 95% CI 0.60–0.95; and ICC 0.84; 95% CI 0.63–0.97; respectively). Both series were significantly higher compared to M_0.6 (median 3; ICC 0.68; 95% CI 0.44–0.80)

and all traditional VMI series ($P ≤ 0.001$), which showed the highest ratings for 70, 80, 90, and 100-keV reconstructions (all medians 3; overall ICC 0.70; 95% CI 0.40–0.81).

Qualitative evaluation image sharpness resulted in the best rating for the 60-keV VMI+ series (median 5) with substantial interrater agreement (ICC 0.63; 95% CI 0.42–0.79) and significant difference in comparison with all other series ($P ≤ 0.023$). Analyses of the traditional VMI series showed highest rating scores at 90 keV (median 4; ICC 0.61; 95% CI 0.41–0.82) regarding subjective image sharpness.

For subjective evaluation of image noise, VMI series reconstructed with 40-keV received the lowest rating scores (median 1; ICC 0.72; 95% CI 0.41–0.84), indicating the highest noise levels. In comparison, 40-keV VMI+ images showed substantially higher ratings (median 3; ICC 0.56; 95% CI 0.33–0.71) indicating a lower image noise level. No significant differences were found between 40-keV VMI+ and M_0.6 images (median 3; $P = 0.180$) regarding image noise. In accordance with the quantitative imaging analysis, image noise ratings subsequently increased from 40 to 100 keV in both VMI and VMI+ reconstructions. Assessment of image noise showed no significant differences in the 90 and 100-keV VMI and VMI+ series ($P ≥ 0.131$).

Results of the subjective image analysis are summarized in Table 2. Examples of the best image series of each reconstruction technique are shown in Figs. 2 and 3. The global ICC score for all three observers was 0.76 (95% CI 0.51–0.88) indicative of a substantial agreement.

Discussion

In this study, we evaluated the impact of monoenergetic reconstructions at various energy levels on quantitative and qualitative image analysis in patients with GISTs at abdominal DECT. In comparison with standard linearly blended and traditional VMI series, we found that VMI+ reconstructions at 40 keV resulted in a higher tumor attenuation and calculated CNR. Furthermore, VMI+ reconstructions at 40 and 50-keV were subjectively found most suitable for lesion delineation, whereas 60-keV VMI+ series received higher ratings regarding overall image quality. Therefore, our data indicate that VMI+ reconstructions should be preferred over traditional VMI and standard linearly blended M_0.6 series for evaluation of GIST lesions and metastases and should be routinely reconstructed when performing DECT of the abdomen.

As DECT generates two CT datasets acquired with different X-ray beam energies, various post-processing algorithms are available to improve image quality. Linearly blended image series are automatically created with usually 60% of the low-keV spectrum and 40% of the high-keV spectrum to simulate standard 120 kV acqui-

Table 2. Comparison of parameters of qualitative image assessment

|	M_0.6	40 VMI	50 VMI	60 VMI	70 VMI	80 VMI	90 VMI	100 VMI	40 VMI+	50 VMI+	60 VMI+	70 VMI+	80 VMI+	90 VMI+	100 VMI+
Image quality	3 (2–5)	2 (1–3)	3 (1–3)	3 (2–4)	4 (2–5)	3 (1–5)	3 (1–5)	3 (2–4)	3 (2–5)	4 (2–5)	5 (3–5)	4 (2–5)	3 (2–5)	3 (2–4)	3 (2–4)
Lesion delineation	3 (1–5)	2 (1–3)	2 (1–3)	3 (1–4)	3 (2–5)	3 (1–4)	3 (1–4)	3 (1–4)	5 (3–5)	5 (2–5)	4 (2–5)	4 (2–4)	4 (2–4)	3 (1–4)	3 (1–5)
Image sharpness	4 (2–5)	2 (1–3)	3 (1–4)	3 (2–4)	3 (2–4)	3 (1–5)	4 (1–5)	3 (2–4)	4 (1–5)	4 (2–5)	5 (3–5)	4 (2–5)	4 (2–5)	4 (3–5)	3 (2–5)
Image noise	3 (1–5)	1 (1–3)	2 (1–3)	2 (1–4)	3 (2–5)	4 (2–5)	5 (2–5)	5 (3–5)	3 (2–4)	3 (2–4)	3 (2–4)	4 (2–5)	4 (2–5)	5 (3–5)	5 (3–5)

Data are given as median with ranges in brackets based on the ratings from three independent observers. Overall image quality, lesion delineation, image sharpness, and image noise were compared between standard linearly blended DECT images (M_0.6), traditional VMI, and noise-optimized VMI+ series in patients with GISTs. Although subjective image quality was rated superior in the 60-keV VMI+ series, the higher attenuation of 40 and 50-keV VMI+ with simultaneously acceptable noise were rated superior for lesion delineation

sition as per the vendor's recommendations and according to other studies [15, 18]. Previous studies have shown that DECT does not increase the radiation dose in abdominal CT examinations compared to single-energy acquisition [24, 25]. Moreover, in this study, we focused on the analysis of virtual monoenergetic reconstructions of abdominal DECT datasets in patients with GISTs. In a previous study, Sudarski et al. demonstrated that traditional VMI reconstructions at 70 keV provide an equivalent objective and an improved subjective image quality compared to polyenergetic images of hepatic metastasis in GIST patients [11]. However, traditional low-keV VMI reconstructions suffer from a high image noise level. The noise-optimized VMI+ algorithm has been designed specifically to overcome this limit and enables a high image contrast without substantial noise [12]. The effects of this new technique in patients with GISTs have not been evaluated so far although visualization of GIST lesions may benefit substantially from improved image contrast.

In the quantitative image analysis, we found that tumor attenuation of GIST lesions and metastases at 40 keV was significantly superior to all other virtual monoenergetic reconstructions and linearly blended series. In addition, we showed that traditional VMI series showed the highest quantitative image parameters at 70 keV which is in accordance with prior studies [11, 26]. In comparison with the noise-optimized VMI+ algorithm, traditional VMI series showed a higher noise level at low-keV reconstruction resulting in lower image quality parameters. These findings are in accordance with previous studies as the VMI+ technique provides increasing iodine CNR with decreasing keV levels and with an optimum CNR obtained at 40 keV [12, 27].

However, the subjective image analysis in our study revealed 60-keV VMI+ series as the image reconstruction of choice regarding subjective image quality and image sharpness. This indicates that the strongest attenuation of GISTs at 40 keV does not automatically result in subjective preference for imaging of GISTs. Based on our results, we would recommend using 60-keV VMI+ in clinical practice rather than linearly blended images or other monoenergetic energy levels in GIST imaging. Reconstruction at 60 keV appears to be a reasonable compromise regarding increased lesion CNR and image noise. However, the optimal VMI+ keV settings need to be re-evaluated in future studies, as well as the impact of VMI+ on diagnostic accuracy.

The result of this study should be interpreted in the context of the study design and consequent limitations. First, we only compared VMI and VMI+ series with linearly blended M_0.6 series as this is the standard linear blending setting on the used DECT system. Other linear blending settings using weighting factors M_0.3 and M_0.5 were not investigated in this study. However, differences in lesion attenuation between M_0.5 and
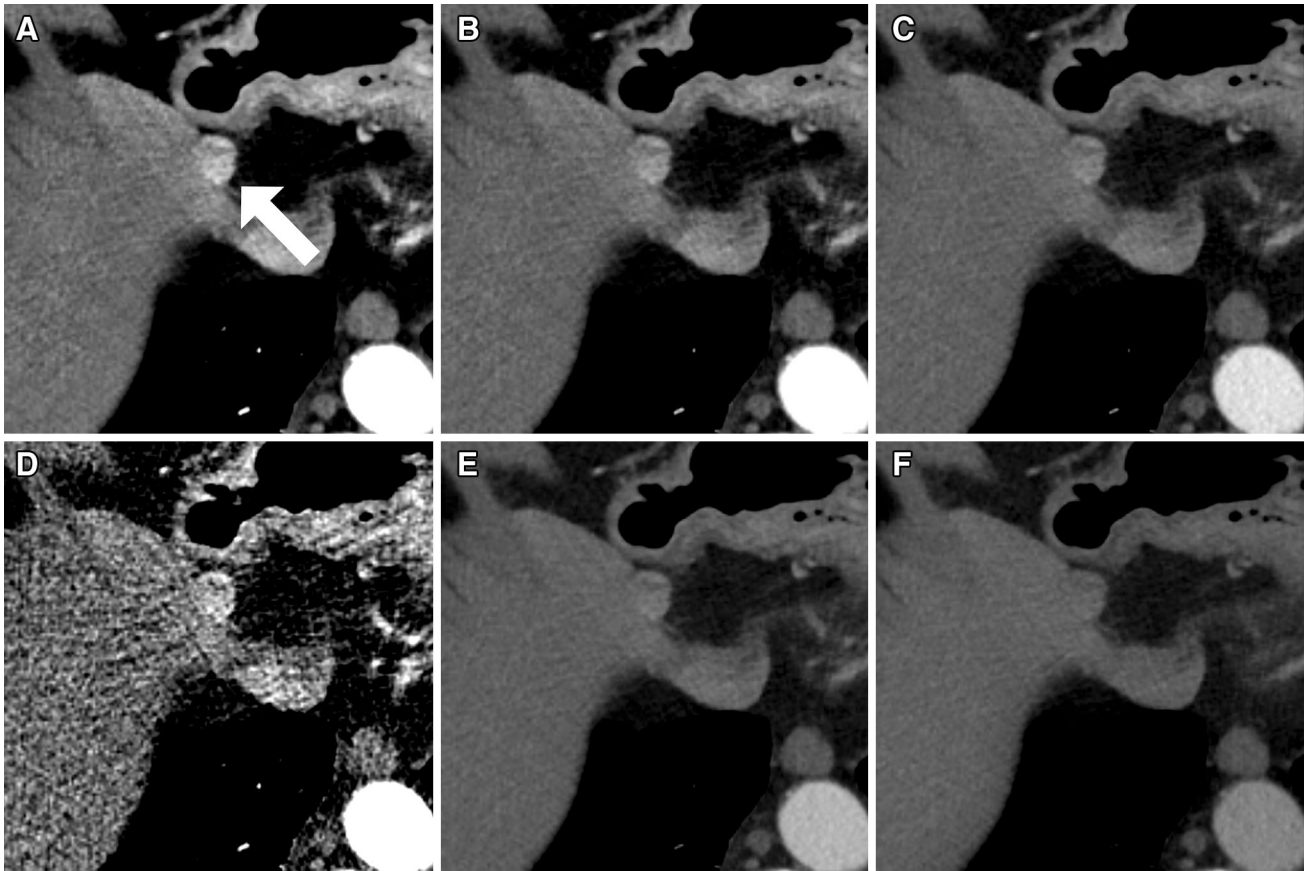
Fig. 2. DECT images of a 52-year-old female patient with histologically proven GIST metastasis of the liver (*arrow*). Images were reconstructed with the noise-optimized VMI+ algorithm at 40 keV (**A**), 50 keV (**B**), and 60 keV (**C**). The VMI+ reconstructions show less image noise than the 40-keV VMI series (**D**), resulting in superior SNR and CNR. Traditional VMI reconstructions showed best quantitative results at 70 keV (**E**). Standard linearly blended M_0.6 image is shown for comparison (**F**). Window settings were as follows: width, 600 HU; level, 150 HU.

M_0.6 linearly blended images can be expected to be less distinct, and these reconstructions have shown superior results regarding image quality compared to M_0.3 reconstructions in previous studies [18, 28]. Second, reviewers were aware that only patients with GIST were included in this study. This might have influenced the ratings especially regarding tumor delineation and lesion enhancement due to a greater diagnostic confidence. Furthermore, evidence of new metastases in GIST patients was solely based on evaluation of prior and follow-up CT examinations. However, every patient had at least one biopsy-proven GIST lesion. Finally, we did not specifically investigate the impact of the VMI+ technique on diagnostic accuracy, although we assume that an improved CNR may result in at least comparable diagnostic accuracy.

In summary, our results demonstrate that the noise-optimized VMI+ algorithm substantially improves subjective and objective image quality of GISTs in abdominal DECT examinations compared to traditional VMI and standard linearly blended images. Based on quantitative and qualitative image quality analysis, we suggest using an energy level of 60 keV for image reconstruction.
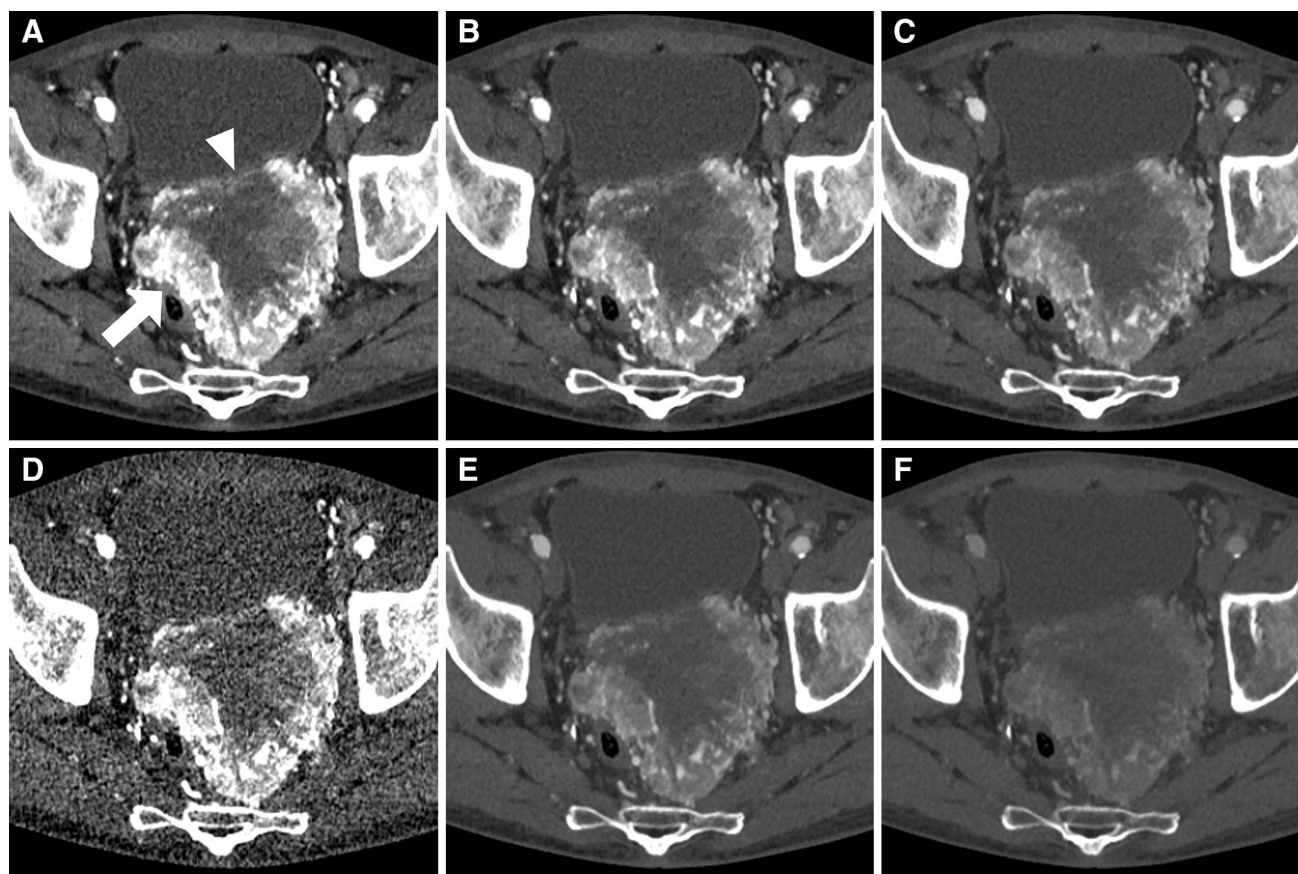
Fig. 3. Axial DECT slices of a 65-year-old male patient with advanced primary GIST of the rectum (*arrow*) and partial response of the central tumor mass (*arrowhead*). Images were reconstructed with the noise-optimized VMI+ algorithm at 40 keV (**A**), 50 keV (**B**), and 60 keV (**C**), which were rated superior in the qualitative image analysis. The highest noise levels were observed in VMI reconstructions at 40 keV (**D**). Traditional VMI series showed the highest qualitative and quantitative parameters at 70 keV (**E**). Linearly blended M_0.6 image is shown for comparison (**F**). Window settings were as follows: width, 400 HU; level, 50 HU.

References

1. Burkill GJ, Badran M, Al-Muderis O, et al. (2003) Malignant gastrointestinal stromal tumor: distribution, imaging features, and pattern of metastatic spread 1. Radiology 226:527–532
2. Joensuu H, Hohenberger P, Corless CL (2013) Gastrointestinal stromal tumour. Lancet 382:973–983
3. DeMatteo RP, Lewis JJ, Leung D, et al. (2000) Two hundred gastrointestinal stromal tumors: recurrence patterns and prognostic factors for survival. Ann Surg 231:51–58
4. Suster S (1996) Gastrointestinal stromal tumors. Semin Diagn Pathol 13:297–313
5. Miettinen M, Lasota J (2001) Gastrointestinal stromal tumors–definition, clinical, histological, immunohistochemical, and molecular genetic features and differential diagnosis. Virchows Arch 438:1–12
6. Mabille M, Vanel D, Albiter M, et al. (2009) Follow-up of hepatic and peritoneal metastases of gastrointestinal tumors (GIST) under Imatinib therapy requires different criteria of radiological evaluation (size is not everything!!!). Eur J Radiol 69:204–208
7. Benjamin RS, Choi H, Macapinlac HA, et al. (2007) We should desist using RECIST, at least in GIST. J Clin Oncol 25:1760–1764
8. Apfaltrer P, Meyer M, Meier C, et al. (2012) Contrast-enhanced dual-energy CT of gastrointestinal stromal tumors: is iodine-related attenuation a potential indicator of tumor response? Investig Radiol 47:65–70
9. Heye T, Nelson RC, Ho LM, Marin D, Boll DT (2012) Dual-energy CT applications in the abdomen. Am J Roentgenol 199:S64–S70
10. Schabel C, Bongers M, Sedlmair M, et al. (2014) Assessment of the hepatic veins in poor contrast conditions using dual energy CT:

evaluation of a novel monoenergetic extrapolation software algorithm. Rofo 186:591–597

11. Sudarski S, Apfaltrer P, Nance JW Jr, et al. (2014) Objective and subjective image quality of liver parenchyma and hepatic metastases with virtual monoenergetic dual-source dual-energy CT reconstructions: an analysis in patients with gastrointestinal stromal tumor. Acad Radiol 21:514–522

12. Grant KL, Flohr TG, Krauss B, et al. (2014) Assessment of an advanced image-based technique to calculate virtual monoenergetic computed tomographic images from a dual-energy examination to improve contrast-to-noise ratio in examinations using iodinated contrast media. Investig Radiol 49:586–592

13. Albrecht MH, Scholtz JE, Kraft J, et al. (2015) Assessment of an advanced monoenergetic reconstruction technique in dual-energy computed tomography of head and neck cancer. Eur Radiol 25:2493–2501

14. Wichmann JL, Noske EM, Kraft J, et al. (2014) Virtual monoenergetic dual-energy computed tomography: optimization of kiloelectron volt settings in head and neck cancer. Investig Radiol 49:735–741

15. Albrecht MH, Scholtz JE, Husers K, et al. (2016) Advanced image-based virtual monoenergetic dual-energy CT angiography of the abdomen: optimization of kiloelectron volt settings to improve image contrast. Eur Radiol 26:1863–1870

16. Frellesen C, Kaup M, Wichmann JL, et al. (2016) Noise-optimized advanced image-based virtual monoenergetic imaging for improved visualization of lung cancer: comparison with traditional virtual monoenergetic imaging. Eur J Radiol 85:665–672

17. Albrecht MH, Trommer J, Wichmann JL, et al. (2016) Comprehensive comparison of virtual monoenergetic and linearly blended reconstruction techniques in third-generation dual-source dual-energy computed tomography angiography of the thorax and abdomen. Investig Radiol 51:582–590

18. Kim KS, Lee JM, Kim SH, et al. (2010) Image fusion in dual energy computed tomography for detection of hypervascular liver hepatocellular carcinoma: phantom and preliminary studies. Investig Radiol 45:149–157

19. Sudarski S, Apfaltrer P, Nance JW Jr, et al. (2013) Optimization of keV-settings in abdominal and lower extremity dual-source dual-energy CT angiography determined with virtual monoenergetic imaging. Eur J Radiol 82:e574–e581

20. Beeres M, Trommer J, Frellesen C, et al. (2016) Evaluation of different keV-settings in dual-energy CT angiography of the aorta using advanced image-based virtual monoenergetic imaging. Int J Cardiovasc Imaging 32:137–144

21. Martin SS, Albrecht MH, Wichmann JL, et al. (2016) Value of a noise-optimized virtual monoenergetic reconstruction technique in dual-energy CT for planning of transcatheter aortic valve replacement. Eur Radiol . doi:10.1007/s00330-016-4422-3

22. De Cecco CN, Caruso D, Schoepf UJ, et al. (2016) Optimization of window settings for virtual monoenergetic imaging in dual-energy CT of the liver: a multi-reader evaluation of standard monoenergetic and advanced imaged-based monoenergetic datasets. Eur J Radiol 85:695–699

23. Shrout PE, Fleiss JL (1979) Intraclass correlations: uses in assessing rater reliability. Psychol Bull 86:420–428

24. De Cecco CN, Darnell A, Macias N, et al. (2013) Second-generation dual-energy computed tomography of the abdomen: radiation dose comparison with 64- and 128-row single-energy acquisition. J Comput Assist Tomogr 37:543–546

25. Wichmann JL, Hardie AD, Schoepf UJ, et al. (2016) Single- and dual-energy CT of the abdomen: comparison of radiation dose and image quality of 2nd and 3rd generation dual-source CT. Eur Radiol . doi:10.1007/s00330-016-4383-6

26. Yamada Y, Jinzaki M, Tanami Y, Abe T, Kuribayashi S (2012) Virtual monochromatic spectral imaging for the evaluation of hypovascular hepatic metastases: the optimal monochromatic level with fast kilovoltage switching dual-energy computed tomography. Investig Radiol 47:292–298

27. Frellesen C, Fessler F, Hardie AD, et al. (2015) Dual-energy CT of the pancreas: improved carcinoma-to-pancreas contrast with a noise-optimized monoenergetic reconstruction algorithm. Eur J Radiol 84:2052–2058

28. Behrendt FF, Schmidt B, Plumhans C, et al. (2009) Image fusion in dual energy computed tomography: effect on contrast enhancement, signal-to-noise ratio and image quality in computed tomography angiography. Investig Radiol 44:1–6